THE JOURNAL OF PHYSICAL CHEMISTRY C
Article
pubs.acs.org/JPCC

Silver-Decorated Cylindrical Nanopores: Combining the Third Dimension with Chemical Enhancement for Efficient Trace Chemical Detection with SERS

Rajesh Kodiyath,[†] Theodoros A. Papadopoulos,[‡] Jian Wang,[§] Zachary A. Combs,[†] Hong Li,[‡] Richard J. C. Brown,[§] Jean-Luc Brédas,[‡] and Vladimir V. Tsukruk*,[†]

[†]School of Materials Science and Engineering, Georgia Institute of Technology, Atlanta, Georgia 30332, United States

[‡]School of Chemistry and Biochemistry and Center for Organic Photonics and Electronics, Georgia Institute of Technology, Atlanta, Georgia 30332, United States

[§]Analytical Science Division, National Physical Laboratory, Teddington, Middlesex, TW11 0LW, United Kingdom

Supporting Information

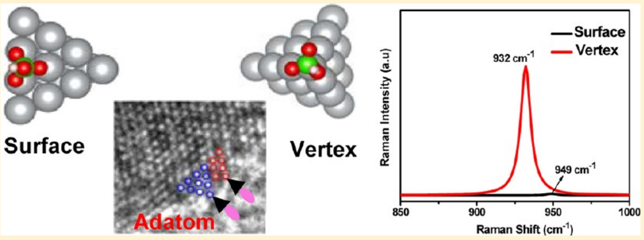

ABSTRACT: We report on the facile fabrication of efficient porous alumina membrane-based SERS substrates that avoid the cumbersome stages of chemical surface modification of the pores and premixing/infiltration of nanoparticles with analytes. The design relies on higher light transmission through the SERS substrates by widening the cylindrical pore diameter to 355 nm and in situ growth of uniform silver nanoparticles on the inner walls. Electromagnetic simulations confirm that the interaction of excitation light with the nanoparticles along the pore walls can be maximized in such a membrane when the nanoparticles are placed within the first 14 μm of the pore depth. For common benchmark Raman analytes such as benzenethiol and Rhodamine 6G, nanomolar detection limits are readily obtained without any additional chemical surface functionalization and/or additional premixing and preconcentration of metal nanoparticles and analytes. Moreover, a high enhancement of 10^6 and a micromolar detection limit are achieved for nonresonant, Raman-stealthy perchloric acid molecules. Quantum mechanical calculations of perchloric acid bound to nanostructured silver clusters with different sizes and binding sites suggest that the maximum chemical enhancement is achieved for molecules located at the tips of the (111) planes of silver lattices, which are abundantly available on the nanoparticles grown in this study.

■ INTRODUCTION

SERS has attracted much attention recently as a highly sensitive probe for the trace level detection of small organic molecules, since the demonstration of single-molecule detection.[1−5] It has also been shown that the SERS technique has great potential for monitoring the fine chemical composition, inner stresses, and trace detection of hazardous molecules.[6−13] The SERS phenomenon is caused by the large electromagnetic field that exist in the small gaps between metal nanostructures, which are called hot spots.[14] The design of the substrate on which the SERS phenomenon becomes significant is the most critical aspect of a sensitive probe for small molecules or biomolecule analytes. Various design strategies have been suggested in order to provide dramatic enhancement for the SERS response with efficient SERS substrates including roughened metal nanoparticle films,[15,16] metallic and bimetallic nanostructures,[17−25] and three-dimensional (3D) porous substrates.[26−29] The highly specific and sensitive detection of liquid and plastic explosives, hazardous chemicals, and biomolecules has been demonstrated using SERS as the detection mechanism, which underlines the significance of this sensing technique.[18,30,31]

For practical applications of SERS-active substrates, the sensitivity of planar metal structures remains modest due to the limited concentration of hot spots available within the laser-activated footprint.[31,32] In contrast, 3D porous substrates show a great potential for increasing the level of enhancement for SERS detection. By extending the sensing substrate into the third dimension, a much greater surface area for particle coverage compared with planar substrates and longer pathway for light propagation are both realized, which could provide opportunities for a greater degree of interaction between hot spots and the incident beam as well as more binding sites for probing molecules.

Efficient 3D SERS substrates have been fabricated using different methods that include the decoration of porous morphology with silver nanostructures on gold-supported polyaniline membranes.[33] Fabrication of periodic 3D metal nanostructures with nanoporosity via colloidal crystal templates was demonstrated in another study,[34] and the resulting structure showed higher SERS activity compared to the two-dimensional (2D) counterpart. Recently, Lee et al. have shown that a variety of 3D nanoparticle structures deposited from

Received: January 27, 2012
Revised: May 31, 2012
Published: June 4, 2012

dx.doi.org/10.1021/jp300902u | J. Phys. Chem. C 2012, 116, 13917−13927

charged aerosols exhibit enhanced SERS efficiency.[35] Photonic crystal fibers[36] and porous membranes with cylindrical nanopores decorated with different metallic nanostructures[37] and periodic nanohole arrays[38] have also attracted great attention due to their large SERS enhancement.

Porous alumina membranes (PAMs) formed by the anodization of aluminum have been used in the fabrication of many functional materials for a number of years because of their unique nanostructures and high density of straight cylindrical pores.[39] The geometrical structures of the PAMs (pore diameters, pore spacings, and membrane thicknesses) can be controlled by the anodization voltage and the electrolytic solution used in the process.[40] PAMs are ideal host templates for metallic nanostructures because of their optical transparency over a wide range of wavelengths.[41] The incident beam can be directed more deeply into the substrate through the wave-guiding properties of ultrathin alumina walls and widely open straight pores,[42,43] adding another element to increase the Raman signal enhancement.

The efficiency of a PAM-based SERS substrate decorated with gold nanoparticles has been previously demonstrated in the label-free detection of plastic explosive materials such as 2,4-dinitrotoluene and 2,4,6-trinitrotoluene down to a record low parts per trillion level.[30] A general design principle has been demonstrated recently to improve the SERS activity of PAM-based SERS substrates with a common Raman marker benzenethiol.[44] Based on the experimentation with PAMs of different pore sizes (100, 255, and 355 nm) decorated with in situ grown silver nanoparticles bound to the pore walls, we have found that SERS substrates with 355 nm pore diameters show higher light transmission compared to that of 100 nm. Higher light transmission results in much improved SERS activity due to multiple photons interactions along the cylindrical pores with a very high enhancement factor, several orders of magnitude better than that reported for traditional 2D substrates.[45−47]

However, the previously discussed procedures for the utilization of efficient planar or porous SERS substrates is overly complex because it includes a cumbersome and not very reliable deposition/filling of nanopores with metal nanostructures and their further functionalization with selectively binding polymer coatings. Moreover, frequently for SERS tests, premixing with analytes is used, which might lead to a gross excess of analytes bound to nanoparticles. Therefore, ways to eliminate these additional steps while preserving high SERS efficiency should be further sought and facilitated by careful analysis of both of the electromagnetic and chemical enhancement mechanisms involved.

Hence, herein, we discuss efficient porous SERS substrates that do not require nanoparticle infiltration and additional polyelectrolyte coating, by applying direct electroless silver nanoparticle growth inside cylindrical pores (Figure 1). These substrates demonstrated high detection efficiency for traditional analytes such as benzenethiol (BT) and Rhodamine 6G (R6G) as well as for a nonresonant molecule, perchloric acid (PA) (Figure 1d); low detection limits were achieved within nanomolar concentration for BT and R6G and micromolar concentration for PA. Electromagnetic simulations using finite element methods (FEM) suggested that the placement of silver nanoparticles within the first 14 μm beneath the surface is critical for the achievement of high efficiency. Furthermore, density functional theory (DFT) calculations demonstrated that the selective chemical binding of PA molecules to the edges of (111) facets of bare silver nanoparticles can facilitate high chemical enhancement. Moreover, since the electroless deposition method does not involve any molecule or polymer as an adherent layer to bind the nanoparticles to the pore walls, the possibility of overlap of the Raman bands of the binding layer with those of the analyte, a common problem for functionalized substrates, is avoided.

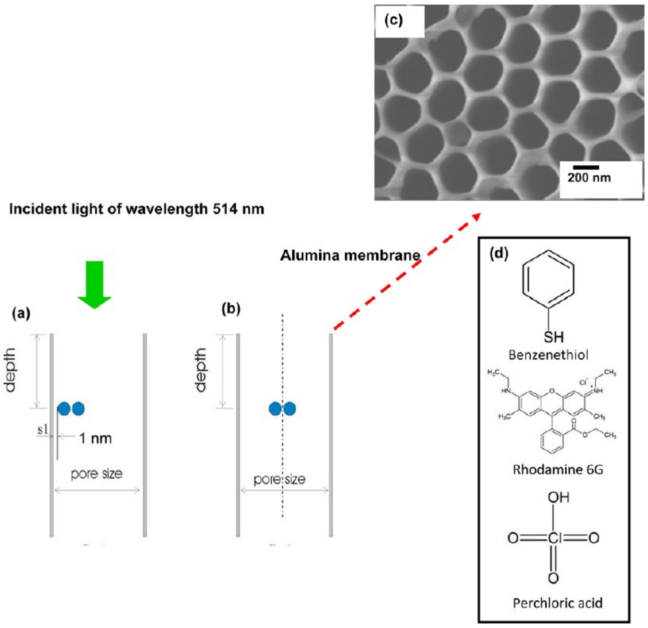

Figure 1. Schematic diagram of the geometries used for the simulation studies (a) dimers at the pore wall and (b) dimers at the center of the pore. The laser light with a wavelength of 514 nm is incident from above, with its polarization parallel to the line joining the centers of the nanoparticles. (c) Porous alumina membrane with pore a diameter of 355 nm synthesized from phosphoric acid electrolyte. (d) Molecular structure of the analytes studied in this work.

■ EXPERIMENTAL SECTION

Synthesis of Porous Alumina Membranes with Different Pore Diameters. A detailed discussion on the PAM fabrication has been reported in the literature (see the Supporting Information).[48−50] Synthesis of the PAMs with different pore diameters (100, 255, and 355 nm) studied here was conducted by using oxalic acid and phosphoric acid as the electrolytes to achieve different pore diameters. Synthesis of PAM with larger pore diameters is damped by the limitations of the electrochemical process. The pore diameter variation at the surface of the membranes is between 7% and 10%, and the ordered domains extend over several micrometers as seen in Figure S1 of the Supporting Information.

Electroless Deposition of Silver Seed and Nanoparticles inside PAMs. Silver nanoparticles were grown on the pore walls following a two-step process.[51] In the first step, the PAMs were immersed in an aqueous solution of $SnCl_2$ (0.02 M) and HCl (0.02 M) for 2 min to deposit Sn^{2+} on the pore walls. The PAMs were then rinsed in Nanopure water and subsequently in acetone and dried. Growth of silver seeds on the pore walls was carried out in the second step by immersing the PAMs in a 0.02 M aqueous solution of $AgNO_3$ for 2 min followed by a second washing step. The deposition of silver nanoparticle seeds was carried out three times to obtain uniform and dense particle coverage on the pore walls. The

PAMs with silver seeds were immersed in 0.5 mL of 10 mM $AgNO_3$ and 1 mL of 100 mM ascorbic acid for 28 min with shaking. The PAMs were then removed from the solution and rinsed thoroughly with Nanopure water so as to remove the particles adhered on the top surface of the PAMs and then dried using nitrogen gas. A detailed growth mechanism and time dependence of particle size distribution were reported elsewhere.[51,52]

Characterization. Substrates were characterized using Hitachi-3400 and Zeiss Ultra60 scanning electron microscopes (SEMs) at an operating voltage of 5−10 keV. High-resolution transmission electron microscopy (HRTEM) images of silver nanoparticles were recorded using a FEI Tecnai F30 TEM with an operating voltage of 300 kV. The TEM samples were prepared by dissolving the SERS substrate in 0.1 M NaOH solution and then subjected to dialysis. The resulting solution was drop cast on a Formvar carbon coated TEM grid.

Atomic force microscopy (AFM) images of the cross section of the PAM (Supporting Information, Figure S3) were collected in tapping mode according to the procedures adapted in our laboratory on a Dimension-3000 microscope (Bruker).[53−55] Silicon nitride tips were used with spring constants of around 50 N m^{-1} and tip radii around 20 nm. AFM scanning was conducted with the rate of 1.0 Hz for surface areas of several micrometers across.

SERS measurements were performed using a WiTec confocal Raman microscope (Alpha 300R) with an Ar^+ ion laser (λ = 514 nm) with 1 mW of intensity of the excitation source according to the usual procedure adapted in our laboratory.[56] The required concentration of R6G and PA solutions was prepared by dissolving the corresponding amount of materials in water, whereas BT was dissolved in the proper amount of ethanol. The SERS substrates with R6G and BT were prepared by immersing the substrate in the solution with a proper concentration for 30 min followed by rinsing. After rinsing, the substrate was dried at room temperature before the measurements. In contrast, the PA solution was drop cast on the SERS substrates and allowed to evaporate for 30 min and not rinsed before the SERS measurements.

Each SERS spectrum was collected with 10 s of exposure time, and at least two exposures were averaged to ensure accurate spectra were recorded. Mapping images were acquired with a lateral resolution of about 300 nm and a vertical resolution of about 1 μm with a 50× objective lens. The UV−vis absorption and transmission spectra of the SERS substrates and neat PAMs were collected using a Craic QDI 202 micro spectrophotometer attached to a Leica microscope.

Electromagnetic Modeling. Simulation studies were carried out by considering silver nanoparticles of 40 nm diameters that are placed in alumina pores with 10 nm wall thickness; parameters close to our experimental values (see the Supporting Information). In all cases, nanoparticle dimers have been considered as these will dominate the maximum response seen for such a system. Nanoparticle dimers have been modeled at various depths within the pores and for two positions: (1) at approximately 1 nm from the pore wall and (2) in the center of the pore (Figure 1). Various pore widths have also been considered. The polarization of the incoming radiation (at 514 nm) was in the incident plane to ensure excitation of the surface plasmons and orthogonal to the line joining the centers of the nanoparticles in the dimers. A schematic diagram of the structures used for the simulation studies is shown in Figure 1.[50] The effect of light waveguiding has not been included in the simulation.

DFT Simulation of the SERS Spectra of Perchloric Acid. Initial silver cluster geometries were taken from the Cambridge Cluster Database[57] and optimized at the B3LYP/LANL2DZ level of theory using the quantum chemistry package Gaussian 09.[58] The geometries of the complex systems, that is, perchloric acid bound to silver clusters of various size (PA−Ag_n, n = 2, 10, 18, and 20), were optimized at the B3LYP/LANL2DZ level of theory for the Ag atoms and at the B3LYP/6-31+G(d) level for the atoms of PA, without the use of vibrational frequency correction factors. Peak assignment was carried out by comparison of the experimental SERS spectra with the theoretical normal Raman intensities (that is, Raman activities) calculated using the same hybrid functional and basis set. This calculation was performed by numerical differentiation of dipole derivatives with respect to the electric field; thus, the theoretical intensity peaks do not involve contributions from factors related to temperature dependence or dependence on the excitation frequency of the laser pulse.[59] We stress that our main goal here is to better understand the trends related to the nonresonant chemical enhancement rather than to perform an extensive theoretical investigation of the various chemical SERS contributions in detail.

■ RESULTS AND DISCUSSION

3D PAM-Based SERS Substrates with in Situ Grown Silver Nanoparticles. High-resolution SEM images of the cross section of the SERS substrates show the distribution of immobilized silver nanoparticles with average diameter of 30 ± 10 nm on the inner walls of the membranes (particle diameter varied within standard deviation for different pores and was 29, 28, and 25 for PAMs with 100, 255, and 355 nm, respectively) (Figure 2; Figures S2 and S3 of the Supporting Information). Nanoparticles with smaller sizes observed on the pore walls are initial silver seeds with a diameter of around 5 nm predeposited for the growth of silver nanoparticles. Although for smaller pore diameters individual nanoparticles are predominantly observed, PAMs with larger pore diameter facilitate the aggregation of silver nanoparticles on the pore walls with predominantly dimers (about 60 nm) formed in addition to individual nanoparticles. The distribution of nanoparticles inside the membranes is not as homogeneous as that observed for substrates fabricated with micro-[60] and nanofabrication[61] techniques, which are limited by high cost and low surface area.[62] High reliability and reproducibility of our SERS substrates is demonstrated in this study (see below).

Analysis of HRTEM images of grown silver nanoparticles shows the presence of (111), (200), (220), and (311) crystallographic planes[63] of the face-centered cubic silver with the edges of the (111) planes mostly exposed at the surface (Figure 3 and Figure S4 of the Supporting Information). The interplanar distance of 0.23 ± 0.01 nm measured here corresponds to the (111) spacing.

Optical Properties of the SERS Substrates. UV−vis absorption spectra and transmission spectra of the silver nanoparticle decorated PAMs with different pore diameters are shown in Figure S5 of the Supporting Information. The optical absorption centered at 460−530 nm is due to the surface plasmon resonance (SPR) of silver nanoparticles with nanoparticle aggregation, as can be concluded from the red shift in plasmon frequency.[64] In addition, the alumina membrane material with refractive index of ∼1.63 may also be responsible

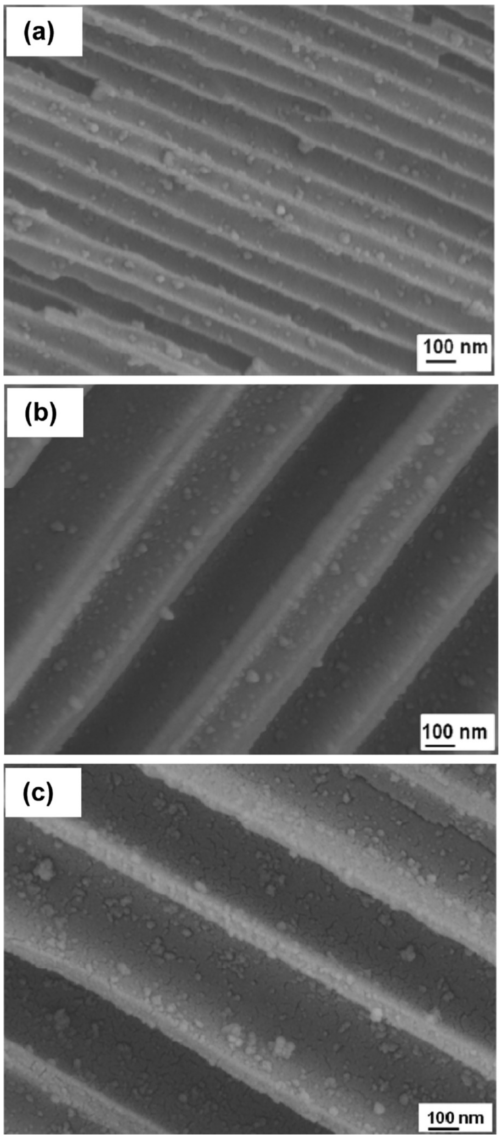

Figure 2. SEM images of silver nanoparticles grown on the porous alumina membranes (cross-sectional view) of (a) 100 nm, (b) 255 nm, and (c) 355 nm pore diameters.

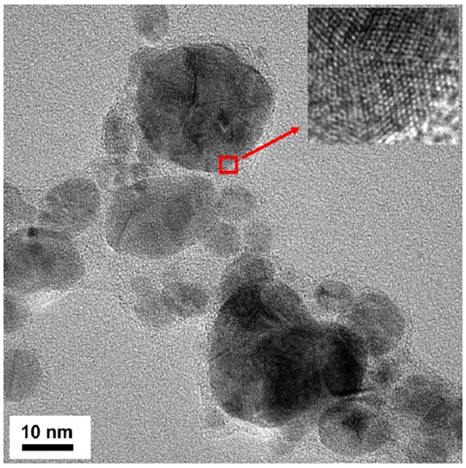

Figure 3. High-resolution TEM image of electroless-deposited silver nanoparticles. Inset image shows the crystallographic planes in the silver nanoparticles.

for the observed red shift.[65,66] The typical plasmon band of 30 nm individual silver nanoparticles in solution is located near 430 nm.[67]

The transmission of silver-decorated PAMs is relatively high in the near-IR range and decreases in the visible region because of scattering.[30] The transmission of the SERS substrates decreases as the pore diameter decreases; SERS substrates with 355 nm pore diameters show the higher transmission in the visible region compared with smaller pore diameters (Supporting Information, Figure S5). SERS substrates with 355 nm pore diameters exhibit transmission of approximately 50% at 514 nm while the substrates with smaller pore diameters show lower transmission (15% and 10% for SERS substrates with 255 and 100 nm pore diameters, respectively).

SERS Activity of Silver Nanoparticle-Decorated PAM-Based Substrates. The SERS activity of the substrate exhibits a strong dependence on the pore diameter of the membranes (Figure 4). The characteristic SERS bands are at 1571 cm^{-1} for BT, related to phenyl ring stretching; 1360, 1504, and 1644 cm^{-1} for R6G, from modes related to the aromatic benzene rings; and 932 cm^{-1} for PA, due to the symmetric stretching mode of Cl−O bonds.[45,68,69] The SERS activity of the substrates is found to be enhanced as the pore diameter increases from 100 to 355 nm as evidenced by the increase in relative intensity of the characteristic peaks of the analyte molecules BT, R6G, and PA adsorbed on the substrates (Figure 4).

The Raman enhancement factor was estimated following the usual procedures reported earlier.[30,70,71] The enhancement factor, EF, has been calculated using the following equation:

$$\mathrm{EF} = \frac{I_{\mathrm{SERS}}}{I_{\mathrm{REF}}} \times \frac{[\mathrm{REF}]}{[\mathrm{SERS}]}$$

where I_{SERS} and I_{REF} are the measured Raman intensities and [SERS] and [REF] are the concentrations of analyte molecules in the SERS and reference samples, respectively. For determining the enhancement factor, the SERS intensity of the characteristic peaks of each analyte (1571 cm^{-1} for BT, 1644 cm^{-1} for R6G, and 932 cm^{-1} for PA, respectively) at different pore depths were extracted from the z-mapping experiments, except for R6G. It was found that the R6G signals are diminished during z-mapping because of decomposition evidenced by the Raman spectra; thus, the Raman intensity from the normal SERS spectra was used for the EF calculation. I_{REF} for the analytes was measured using solid R6G and BT specimens and PA liquid deposited on a silicon wafer. The enhancement factor was estimated using the solution concentration (g/mL) of the analyte and reference sample used for the measurements. As known, this approach underestimates the enhancement factor, since only an unknown fraction of the molecules actually end up on silver nanoparticles, and hence, the numbers reported here actually represent a lower-bound, very conservative estimate.

The enhancement factor obtained for BT and R6G is about $\sim 10^{10}$ on substrates with 355 nm pore diameters. The observed enhancement factor lower-bound value is four orders of magnitude higher than that commonly reported for traditional 2D substrates of gold and silver nanostructures.[45−47,72−74] The enhancement factor for nonresonant PA molecules is close to 10^6 and is about two orders of magnitude better than what is reported for traditional 2D silver substrates.[75]

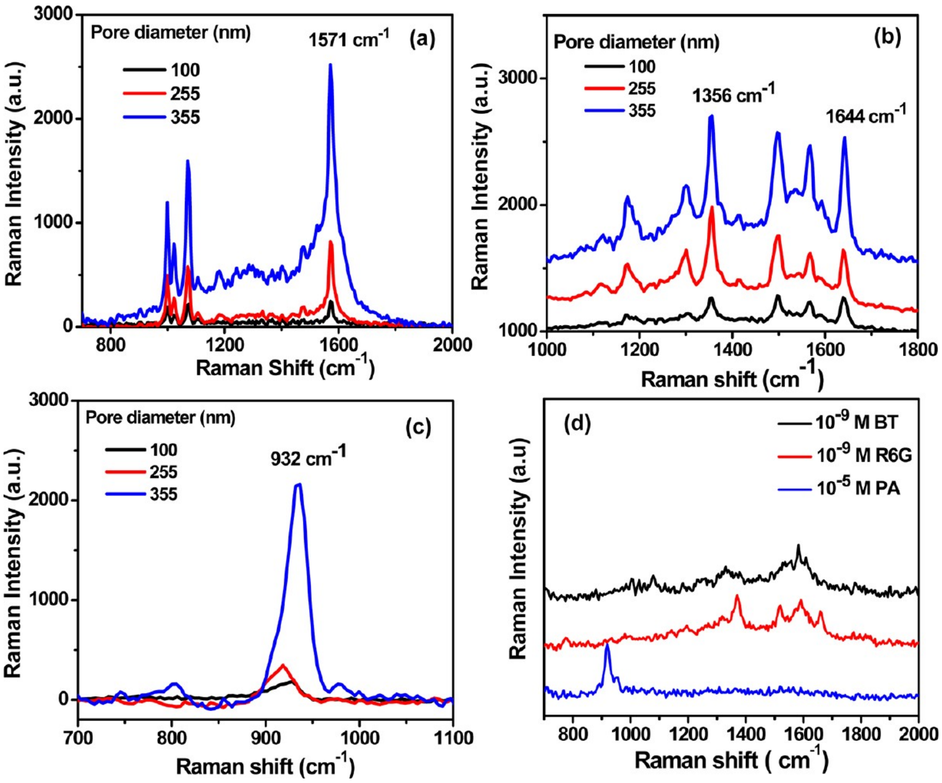

Figure 4. SERS spectra of (a) 10^{-6} M BT, (b) 10^{-7} M R6G, and (c) 10^{-3} M PA on each of the porous alumina membranes. (d) SERS spectra of 10^{-9} M BT and R6G and 10^{-5} M PA (the spectra were recorded using substrates of 355 nm pore diameters).

Correspondingly, a low detection limit observed for these substrates was 10^{-9} M for BT and R6G and 10^{-5} M for PA without using any binding agent and special sample preparations to facilitate the adsorption of analytes that are usually exploited in literature. Again, we emphasize that, in contrast to most of the reported studies, analytes were deposited on the substrate from solution instead of premixing the nanoparticles and analyte to control the surface coverage and dramatically increase local presence of analytes.[76,68,77] It is important to note that, in most of the perchlorate detection studies, the nanoparticle surface is functionalized with positively charged molecules to facilitate the adsorption of perchlorate ions on the nanoparticle surface in contrast to our substrate with direct adsorption of the PA molecules onto bare nanoparticles.[75,69]

Furthermore, we conducted complete Raman mapping in xy-directions as well as in z-direction in order to understand the SERS phenomena that occur in 3D porous structures (Figure 5). The mapping was conducted by monitoring the intensity of the 1571 and 932 cm^{-1} peaks of BT and PA, respectively, through the depth (z-direction) of the porous alumina membranes. The Raman intensity of the analytes gradually decreases as the depth of measurement increases away from the top surface of the substrate. Since the transmission of light is higher for SERS substrates with larger pore diameters, these substrates are expected to show higher SERS intensity for greater depths from the surface of the PAM despite slight decrease in a number of nanoparticles within a laser footprint.

In fact, we observed that the largest SERS enhancement occurs within 5 and 8 μm regions near the surface of the PAM for the substrates with 100 and 255 nm pore diameters, respectively (Supporting Information, Figure S6). However, SERS substrates with 355 nm pore diameters show the highest

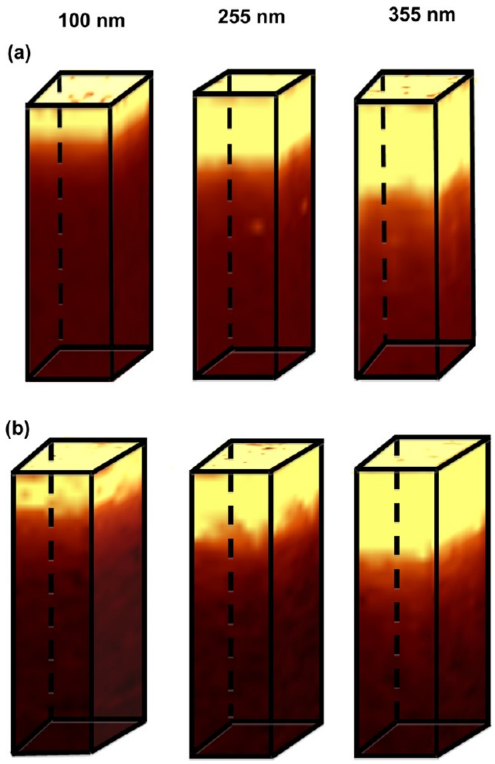

Figure 5. Confocal SERS mapping of (a) 1571 cm^{-1} peak of BT and (b) 932 cm^{-1} peak of PA through the depth of the porous alumina membranes with different pore diameters. The 3D images were constructed from the experimental xy and z-mapping (Supporting Information, Figure S6 (scan depth = 40 μm and scan width = 10 μm) and Figure S7).

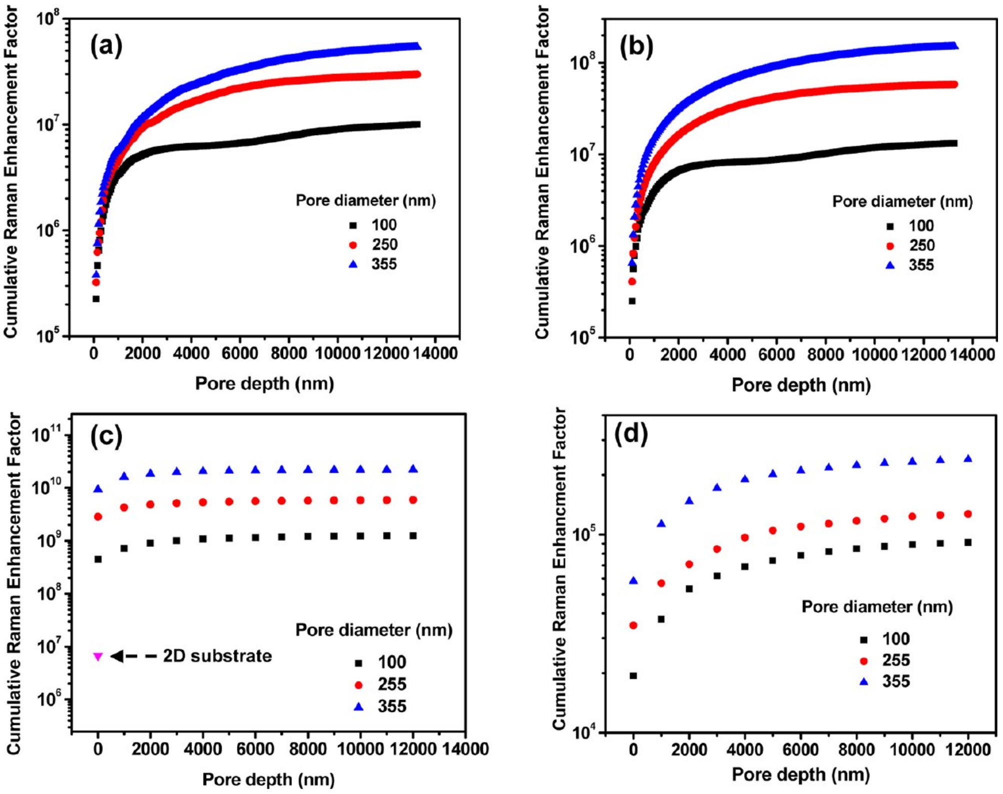

Figure 6. Variation of cumulative Raman enhancement factor extracted from electromagnetic simulation for different pore diameters with a silver nanoparticle dimer placed (a) at pore wall and (b) at center of pore. Cumulative Raman enhancement factor obtained from experimental z-mapping for (c) BT (enhancement factor form a 2D SERS substrate is also included for comparison) and (d) PA with substrates of different pore diameters. (Panels b and c reproduced with permission from ref 44, copyright Wiley-VCH).

SERS intensity over a 10−14 μm region from the surface of the PAMs. Based on the Raman mapping experiment in the z-direction, it can be concluded that PAM-based SERS substrates with larger pore diameters show higher light transmission through the channels. As a result, the excitation of silver nanoparticles occurs at greater depths through the PAMs, which in turn improves the SERS activity of substrates with larger pore diameters.

The homogeneity of the substrates in the xy-plane was further investigated by mapping the characteristic Raman band of the analytes on the substrates; uniform SERS signals were obtained over the entire region within ±25% from pore to pore (Supporting Information, Figure S7). The reproducibility was tested for three batches of substrates (Supporting Information, Figure S8). The SERS intensity was found to be very reproducible at different locations within a substrate as well as between substrates. The SERS intensity varies within ±7% between substrates, which indicates the high homogeneity of the SERS substrates despite the variation in local wall coverage with nanoparticles aggregates.

Electromagnetic Modeling of Raman Enhancement in Cylindrical Pores. To understand the pore size dependence of the SERS activity, we have simulated the Raman enhancement using silver nanoparticle dimers under different conditions.[50] Dimers are chosen for the modeling, since they are the predominant aggregates observed on the pore walls (Supporting Information, Figure S2). Larger nanoparticle aggregates are not considered in this study even though higher aggregates would give an equally large enhancement over a larger area but will not actually increase the maximum enhancement observed.[78,79] Silver nanoparticles were placed in the pores with an orientation that provides maximum enhancement between nanoparticles (see "hot spot" in Figure S9a, b of the Supporting Information). Dimers with other orientations and separations are not discussed here, since they provide only minor contributions (Supporting Information, Figure S9c). In all cases, the predicted enhancement is of a similar order of magnitude as the enhancement level expected from a silver dimer.[80,81] This result implies that the majority of the enhancement is coming from the silver dimers and that there is no significant enhancement effect coming from the pore itself (Supporting Information, Figure S9d). Thus, the role of the pore is to constrain the incident radiation in such a manner that the maximum enhancement can be realized at certain widths.

A series of electromagnetic field peak intensities is observed along the main axis of the cylindrical pores with spacing close to $\lambda/2$ (Supporting Information, Figure S10). It is evident that significant electromagnetic enhancement occurs for nanoparticle dimers placed several micrometers beneath the surface, which is in good agreement with the experimental z-mapping (Figures 5 and S6 of the Supporting Information). The observed enhancement is smaller for dimers located close to the pore wall and shows much less periodicity as a function of depth into the pore. In both cases, this is believed to be related to the damping effect of the aluminum oxide walls on the incident light. The periodicity related to interference of the wavelength of the incident light with the width of the pore is apparent throughout the modeling; however, this is a lot less clear when the dimer is close to the pore wall, due to the interfering effect of the alumina at the side of the pore. For the dimer placed at the center of the pore, the periodic variation associated with the wavelength of the light is initially much larger than any change linked to depth within the pore. However, at larger depth, the attenuation begins to dominate with enhancement decreasing by an order of magnitude (Supporting Information, Figure S10).

The simulations suggest that the electromagnetic enhancement achieves a maximum at 400−450 nm pore width before decreasing again as the pore gets wider. A membrane with 400 nm diameter is optimum for the pore to act as an efficient waveguide for the incident light. Any narrower than this and the light is unable to pass deep into the pore effectively; any wider than this and there might start to be some significant reflections and destructive interference of the light.

To compare the experimental results and the simulated Raman enhancement factors, we extracted the Raman intensity (signal intensity that was higher than the noise level by a factor of 3) from the z-mapping of the substrates with different pore diameters at various pore depths. The Raman enhancement factors from both experiments and simulations for different pore depths are plotted in Figure 6. The overall enhancement from each of the substrate was estimated by adding Raman enhancement at different depths (1 μm interval) from the top surface of the substrates. The integrated Raman enhancement gradually increases with accumulated nanoparticles along the pore depths (Figure 6a, b). The cumulative enhancement factor shows saturation at depth higher than 10−14 μm. In agreement with the results of the simulations, the experimental observations also point to the fact that the SERS substrates fabricated from 355 nm pore diameters show high SERS activity with saturation at depths of 10−14 μm (Figure 6c, d). For BT, the experimental enhancement factor is two orders of magnitude higher than that calculated from the electromagnetic simulation. This additional increase can be attributed to the chemical enhancement (which can reach 10^3) for BT molecules chemisorbed on silver surface that were not included in the simulation.[82] However, the enhancement factor obtained for PA is lower than the theoretically predicted enhancements. This may be due to the low surface coverage of PA in the hot spots and the low binding affinity of PA to silver nanoparticles.

To compare the SERS activity of the PAM-based SERS substrates with traditional 2D substrates, we have included enhancement factor for BT obtained from a 2D SERS substrate fabricated from silver nanoparticles[83] (particle size is 30 ± 5 nm[18]) drop cast on a silicon wafer under similar conditions (Figure 6c). The enhancement factor measured in this case is close to 10^7 and is in good agreement with the reported enhancement values thus confirming the robustness of our measurements and evaluation approaches.[45−47]

It is important to note that the enhancement factor reported here is a cumulative enhancement factor obtained by adding enhancement at different depths that is an added advantage for PAM-based 3D substrates. The higher SERS activity of the PAM-based SERS substrate could be attributed to the excitation of additional nanoparticles in the third dimension due to the combined effect of light transmission and waveguiding properties associated with the transparent alumina membranes that are absent in traditional 2D substrates with a small fraction of photons interacting with a single layer of nanoparticles.

DFT Simulation of Chemical Enhancement. As is well established, in addition to electromagnetic field enhancement, SERS also shows chemical enhancement (CM), which is driven by the combined effect of three contributions, namely, a charge transfer (CT) mechanism,[84] a molecular resonance (RRS) mechanism,[85] and a nonresonant chemical (CHEM) mechanism.[86] The CT and RRS mechanisms arise when the incident radiation is in resonance with a molecule-to-metal or metal-to-molecule electronic transition and a molecular excitation, respectively; when activated, they can contribute to a major extent toward the total enhancement by a factor of $10-10^6$.[85] The CHEM mechanism, on the other hand, occurs due to the bonding interactions between the molecule and the metal surface, allowing relaxation of the electronic structure and giving rise to enhancements on the order of $10-10^2$.[85] Even though the difference in the nature of these enhancement mechanisms has been well identified and characterized over the years, a separation of their effect is not straightforward[87]

In this section, we try to elucidate the factors leading to a CHEM enhancement in the case of PA (we note that PA is unlikely to present resonance-enhancement contributions; in addition, much higher-level calculations would be needed to reliably address the possibilities for resonance enhancement, which is beyond the scope of the present study). We seek to extract valuable information from an analysis of the electronic structure, bonding interactions, and Raman spectra of PA as it binds on silver clusters of various sizes. Figure S11 of the Supporting Information shows the optimized geometries of the complexes formed by the interaction of PA with different silver clusters denoted as PA−Ag_n (n = 2, 10, and 18). PA is found to bind to the metal clusters through an oxygen atom. In terms of geometry, the oxygen involved in the binding is calculated to preferentially locate directly over an Ag atom rather than over a hollow site, with a total energy difference between on-site and hollow-site bonding of about 0.05 eV.

Due to the bonding interaction between PA and the metal surface as well as the subsequent relaxation of the electronic structure of the complex, there occurs some redistribution of charge. The amount of partial charge transferred from PA to the silver cluster is tabulated in Table 1 for each of the three complexes and was estimated via a natural population analysis. The results in Table 1 indicate that the amount of charge transfer to the silver cluster increases with the cluster size, which gives rise to an increase in the induced static electronic polarizability α calculated for the PA−Ag_n complexes (Table 1). This quantity is defined as[88]

Table 1. Calculated Induced Static Polarizability and O−Ag Bond Length for PA and Ag_n−PA (n = 2, 10, 18)

system	induced static polarizability ($nm^3 \times 10^{-3}$)	bond length (O−Ag) (nm)	partial charge on cluster (|e|)
PA	–	–	–
Ag_2−PA	1.55	0.277	−0.011
Ag_{10}−PA	5.12	0.277	−0.053
Ag_{18}−PA	6.60	0.266	−0.061

$$\alpha[\text{induced}] = \alpha(\text{PA}-\text{Ag}_n) - \alpha(\text{Ag}_n) - \alpha(\text{PA})$$

and reflects the degree of interaction between the organic and metal components in the complex as well as the increased ability of the system to be Raman active. Thus, it is expected that complexes of larger sizes will show even higher enhanced Raman intensity.

The calculated Raman spectra of PA and the PA−Ag_n complexes are shown in Figure 7a. The Raman band at 927 cm^{-1} is due to symmetrical stretching of the Cl−O bonds, as

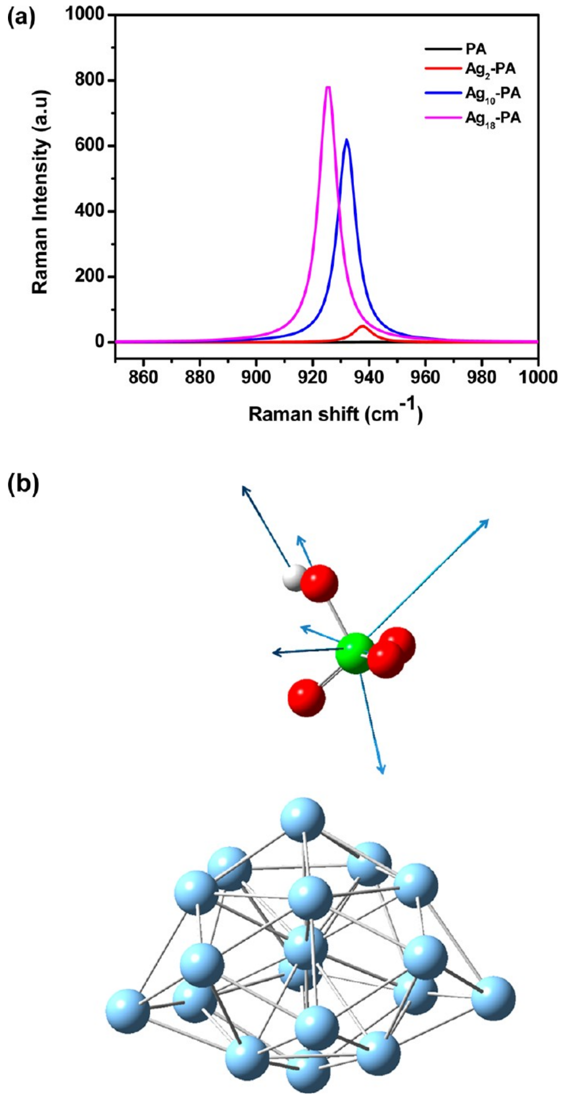

Figure 7. (a) DFT-computed Raman intensity for perchloric acid and perchloric acid−silver complexes. (b) Displacement vectors corresponding to the 927 cm^{-1} band in the Ag_{18}−PA complex.

indicated by the displacement vectors of PA attached to an 18 atom cluster (Figure 7b). We observe that the silver atoms do not contribute to any significant Raman band. The intensity of the characteristic Raman band increases with cluster size, as expected (Figure 7a).

Analysis of the O−Ag bond length in each of the clusters shows that it becomes shorter as the cluster size increases (Table 1). This points to stronger interactions between molecule and surface, related to the dative bond coming from an oxygen lone pair. Thus, the charge transfer increases with cluster size, which in turn increases the induced polarizability[89] and promotes the enhancement of the Raman intensity. Also, it is interesting to note that the Raman band of the isolated PA molecule shifts to a lower frequency (from 945 to 925 cm^{-1}) when PA attaches to silver clusters of increasing size. This red shift in the vibration frequency is related to the shortening of the O−Ag bond with cluster size as confirmed by calculating the Raman frequency of the PA−Ag_{18} complex for various O−Ag bond lengths (Table 1). The calculated range of Raman peak positions is in very good agreement with the experimental SERS spectrum obtained with silver nanoparticles (932 cm^{-1}).

Several theoretical studies have shown that the enhancement mechanism of tetrahedral Ag_{20} clusters is comparable to that of large silver nanoparticles of diameter greater than 10 nm.[90,91] For instance, it has been shown that, for pyridine, the properties calculated for the Ag_{20}−pyridine surface complex show good agreement with experimental results.[92] To understand the effect of different binding sites on the Raman spectra, we have simulated two limiting cases of binding configurations for PA on a tetrahedral Ag_{20} cluster: a surface-type complex (S-complex) and a vertex-type complex (V-complex); the optimized binding geometries are displayed in Figure 8. In the vertex complex, the PA molecule binds to the metal cluster via a single oxygen atom with a Ag−O bond length of 0.279 nm (Table 2); in the surface complex, the PA molecule interacts with the metal cluster via three oxygen atoms and presents a much larger average Ag−O distance of 0.391 nm (Table 2). The large differences in binding geometry and atomic distances lead to markedly different interactions between the PA

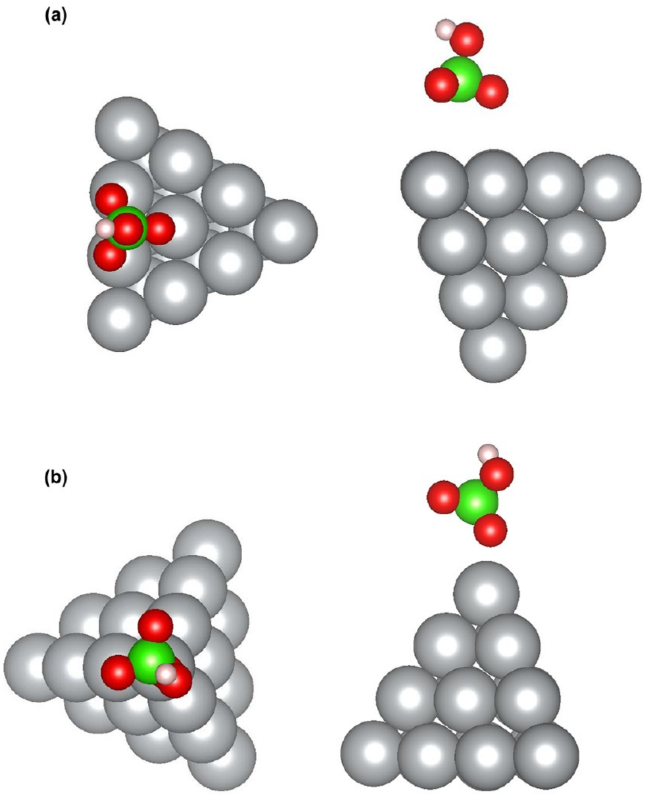

Figure 8. Top and side views of perchloric acid in (a) a surface configuration, and (b) a vertex configuration on a Ag_{20} tetrahedral cluster.

Table 2. Calculated Induced Static Polarizability and O−Ag Bond Length for a Tetrahedral Configuration of the PA−Ag_{20} Complex

system	induced static polarizability ($nm^3 \times 10^{-3}$)	bond length (O−Ag) (nm)	partial charge on cluster (|e|)
Ag_{20}−PA (surface)	0.57	0.391	−0.069
Ag_{20}−PA (vertex)	10.2	0.279	−0.112

molecule and the metal cluster, which ultimately contributes to distinct vibrational characters for the two complexes.

As shown in Figure 9, the Raman intensity enhancement for the vertex complex is about two orders of magnitude larger as compared to the surface complex; a blue shift in the Raman frequency from 932 cm^{-1} for the V-complex to 949 cm^{-1} for the S-complex is calculated, due to the largely increased Ag−O distance. A similar CHEM enhancement simulation was reported in earlier works for BT and R6G.[82,93,94] We note that the overall enhancement factor of 10^6 obtained experimentally for PA is lower than the theoretically predicted enhancement coming from the combined contribution of EM and CHEM; this discrepancy is likely due to the low surface coverage of PA in the hot spots in contrast to optimistic suggestion.

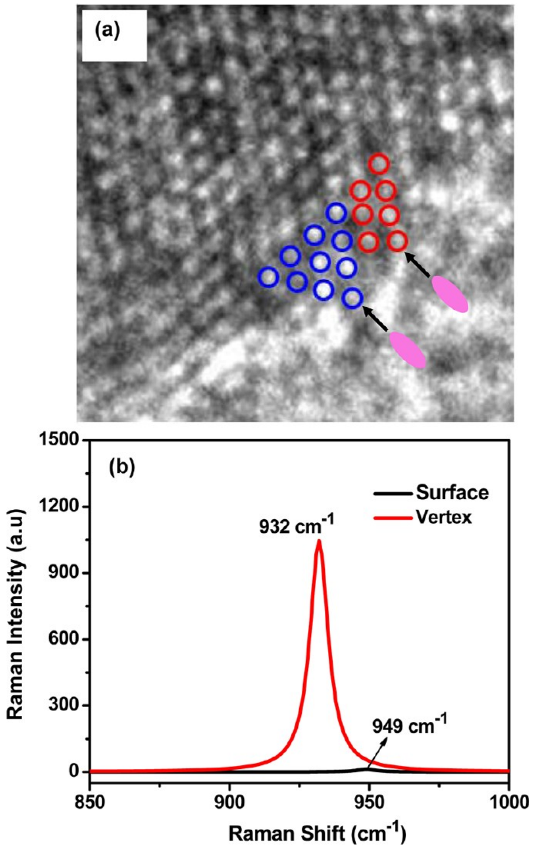

Figure 9. (a) HRTEM image showing the presence of adatoms at the surface of the silver nanoparticles (the binding of PA to the nanoparticle surface is illustrated schematically). (b) Simulated Raman intensity for the surface and vertex complexes of perchloric acid on Ag_{20} clusters.

As discussed previously,[85,95] the CHEM factor can be attributed to the ground-state interaction of the molecule with the metal. This can be understood by comparing the magnitude of charge transfer and induced static polarizability for the two complexes. As given in Table 2, the amount of charge transfer for the V-complex is nearly twice as large as the charge transfer for the S-complex, leading to a ∼20-time increase in induced static polarizability.

Based on the large differences in Ag−O bond lengths between the Ag_{20} surface and vertex complexes, PA can be considered to be physisorbed on the cluster in the surface complex while the PA molecules in the vertex complex can be considered as weakly chemisorbed (Figure 8).[92] From this perspective, the V-complex can also be viewed as an adatom or adparticle structure, which is regarded as crucial for short-range chemical enhancements.[96−98] In the case of the silver nanoparticles investigated in this work, it is more likely to have adparticles on the edges of the (111) surface rather than on an ideally clean (111) surface, as illustrated on HRTEM images in Figure 9. Analysis of these two figures suggests the presence of edges of (111) crystallographic planes at the surfaces. In order to reach the state of thermodynamic stability, crystal faces with higher free energies, such as (110) and (311), will grow faster and will hardly be present at the surface in large proportion.[99,100] On the other hand, crystal faces with lower free energies such as the family of (111) planes will dominate the nanoparticle surface. We suggest that, in our experiments, the adsorption of PA on the edges of the (111) plane is the most probable configuration.

■ CONCLUSIONS

In conclusion, we have demonstrated PAM-based substrates exhibiting high Raman enhancement factors by tuning the transmission of light and deposition of nanoparticles on cylindrical nanopores. Silver nanoparticle-decorated PAMs with different pore diameters of 100, 255, and 355 nm were synthesized by varying the anodization conditions such as electrolytes and applied voltages. The Raman enhancement factors for the substrates with 355 nm pore diameter are very high and close to 10^{10} for common Raman markers and 10^6 for the nonresonant perchloric acid molecule. The Raman enhancements observed here are several orders of magnitude higher than those reported for traditional 2D substrates.

Our work offers a general strategy to optimize the fabrication of PAM-based SERS substrates that show high SERS activity. The electromagnetic simulations of silver nanoparticle dimers inside the alumina membranes with different pore diameters helped in the design of PAM-based SERS substrates with optimum pore sizes to enhance the SERS activity. As suggested by the electromagnetic simulations, deposition of nanoparticles mostly within the first 14 μm from the surface is important in achieving enhanced SERS response. Furthermore, DFT calculations provided further insight regarding the favorable orientation and binding site of perchloric acid molecules as they attach to silver nanoparticles, the Raman band positions and associated Raman-active modes, as well as understanding of fine details of analyte−metal interaction and its effect on the chemical enhancement.

We believe that our approach provides an efficient pathway to the rational development of open nanoporous designs, which can allow the detection of trace concentrations of not just known Raman markers, but also practical target molecules such as plastic explosives, hazardous chemicals and gases, and biomarkers with low Raman cross sections.

■ ASSOCIATED CONTENT

Ⓢ Supporting Information

Porous alumina synthesis procedures, electromagnetic modeling details, SEM images, histograms showing silver nanoparticle size distribution, AFM image, HRTEM images, absorption spectra, confocal SERS mapping, Raman mapping, figures of variation of SERS intensity and electric field distribution for silver nanoparticles, representative Raman enhancement patterns, sketches of DFT-optimized structures, and references.

This material is available free of charge via the Internet at http://pubs.acs.org.

AUTHOR INFORMATION

Corresponding Author

*E-mail: vladimir@mse.gatech.edu.

Notes

The authors declare no competing financial interest.

ACKNOWLEDGMENTS

Financial support from the NSF-CBET 0930781 project, the DARPA/US Army W31P4Q10C0027 grant through a subcontract from EngeniusMicro, and the NSF-STC Program DMR-0120967 is gratefully acknowledged. Z. A. Combs thanks the support by the National Defense Science and Engineering Graduate (NDSEG) Fellowship, 32 CFR 168a. The authors would like to thank M. Gupta for help with PAM fabrication and S. Mukhopadhyay for useful discussions. The HRTEM used in this work is supported by funding from DMR 0922776.

REFERENCES

(1) Nie, S. M.; Emory, S. R. *Science* **1997**, *275*, 1102.
(2) Kneipp, K.; Wang, Y.; Kneipp, H.; Perelman, L. T.; Itskan, I.; Dasari, R.; Feld, M. S. *Phys. Rev. Lett.* **1997**, *78*, 1667.
(3) Camden, J. P.; Dieringer, J. A.; Wang, Y.; Masiello, D. J.; Marks, L. D.; Schatz, G. C.; Van Duyne, R. P. *J. Am. Chem. Soc.* **2008**, *130*, 12616.
(4) Kneipp, K.; Kneipp, H.; Deinum, G.; Itzkan, I.; Dasari, R. R.; Feld, M. S. *Appl. Spectrosc.* **1998**, *52*, 175.
(5) Kleinman, S. L.; Ringe, E.; Valley, N.; Wustholz, K. L.; Phillips, E.; Scheidt, K. A.; Schatz, G. C.; Van Duyne, R. P. *J. Am. Chem. Soc.* **2011**, *133*, 4115.
(6) *Surface-Enhanced Raman Scattering Physics and Application*; Kneipp, K., Moskovits, M., Kneipp, H., Eds.; Springer: New York, 2006.
(7) Schlucker, S. *Surface Enhanced Raman Spectroscopy: Analytical, Biophysical and Life Science Applications*; Wiley-VCH: Weinheim, Germany, 2011.
(8) Baker, G. A.; Moore, D. S. *Anal. Bioanal. Chem.* **2005**, *382*, 1751.
(9) Lee, S. J.; Moskovits, M. *Nano Lett.* **2011**, *11*, 145.
(10) Kneipp, K.; Kneipp, H.; Itzkan, I.; Dasari, R. R.; Feld, M. S. *Chem. Rev.* **1999**, *99*, 2957.
(11) Jiang, C.; Lio, W. Y.; Tsukruk, V. V. *Phys. Rev. Lett.* **2005**, *95*, 115503.
(12) Kharlampieva, E.; Tsukruk, T.; Slocik, J. M.; Ko, H.; Poulsen, N.; Naik, R. R.; Kröger, N.; Tsukruk, V. V. *Adv. Mater.* **2008**, *20*, 3279.
(13) Singamaneni, S.; Kharlampieva, E.; Jang, J.-H.; McConney, M. E.; Jiang, H.; Bunning, T. J.; Thomas, E. L.; Tsukruk, V. V. *Adv. Mater.* **2010**, *22*, 1369.
(14) Thaxton, C. S.; Elghanian, R.; Thomas, A. D.; Stoeva, S. I.; Lee, J. S.; Smith, N. D.; Schaeffer, A. J.; Klocker, H.; Horninger, W.; Bartsch, G.; Mirkin, C. A. *Proc. Natl. Acad. Sci. U.S.A.* **2009**, *106* (44), 18437.
(15) Freeman, R. G.; Grabar, K. C.; Allison, K. J.; Bright, R. M.; Davis, J. A.; Guthrie, A. P.; Hommer, M. B.; Jackson, M. A.; Smith, P. C.; Walter, D. G.; Natan, M. J. *Science* **1995**, *267*, 1629.
(16) Wang, Z.; Pan, S.; Krauss, T. D.; Du, H.; Rothberg, L. J. *Proc. Natl. Acad. Sci. U.S.A.* **2003**, *100*, 8638.
(17) Lee, C. H.; Tian, L.; Singamaneni, S. *ACS Appl. Mater. Interfaces* **2010**, *2*, 3429.
(18) Combs, Z. A.; Chang, S.; Clark, T.; Singamaneni, S.; Anderson, K. D.; Tsukruk, V. V. *Langmuir* **2011**, *27*, 3198.
(19) Chang, S.; Ko, H.; Gunawidjaja, R.; Tsukruk, V. V. *J. Phys. Chem. C* **2011**, *115*, 4387.
(20) Banholzer, M. J.; Millstone, J. E.; Qin, L. D.; Mirkin, C. A. *Chem. Soc. Rev.* **2008**, *37*, 885.
(21) Hulteen, J. C.; Treichel, D. A.; Smith, M. T.; Duval, M. L.; Jensen, T. R.; Van Duyne, R. P. *J. Phys. Chem. B* **1999**, *103*, 3854.
(22) Gunawidjaja, R.; Peleshanko, S.; Ko, H.; Tsukruk, V. V. *Adv. Mater.* **2008**, *20*, 1544.
(23) Qin, L.; Zhou, S.; Xue, C.; Atkinson, A.; Schatz, G. C.; Mirkin, C. A. *Proc. Natl. Acad. Sci. U.S.A.* **2006**, *103*, 13300.
(24) Gobin, A. M.; Lee, M. H.; Halas, N. J.; James, W. D.; Drezek, R. A.; West, J. L. *Nano Lett.* **2007**, *7*, 1929.
(25) Gupta, M. K.; Chang, S.; Singamaneni, S.; Drummy, L. F.; Gunawidjaja, R.; Naik, R. R.; Tsukruk, V. V. *Small* **2011**, *7*, 1192.
(26) Chan, S.; Kwon, S.; Koo, T.; Lee, L.; Berlin, A. A. *Adv. Mater.* **2003**, *15*, 1595.
(27) Ko, H.; Singamaneni, S.; Tsukruk, V. V. *Small* **2008**, *4*, 1576.
(28) Qian, L. H.; Ding, Y.; Fujita, T.; Chen, M. W. *Langmuir* **2008**, *24*, 4427.
(29) He, H.; Cai, W.; Lin, Y.; Chen, B. *Chem. Commun.* **2010**, *46*, 7223.
(30) Ko, H.; Chang, S.; Tsukruk, V. V. *ACS Nano* **2009**, *3*, 18.1.
(31) Chang, S.; Ko, H.; Singamaneni, S.; Gunawidjaja, R.; Tsukruk, V. V. *Anal. Chem.* **2009**, *81*, 5740.
(32) Ko, H.; Tsukruk, V. V. *Small* **2008**, *4*, 1980.
(33) Xu, P.; Mack, N. H.; Jeon, S. H.; Doorn, S. K.; Han, X.; Wang, H. L. *Langmuir* **2010**, *26*, 8882.
(34) Tessier, P. M.; Velev, O. D.; Kalambur, A. T.; Rabolt, J. F.; Lennhoff, A. M.; Kaler, E. W. *J. Am. Chem. Soc.* **2000**, *122*, 9554.
(35) Lee, H.; You, S.; Pikhitsa, P. V.; Kim, J.; Kwon, S.; Woo, C. G.; Choi, M. *Nano Lett.* **2011**, *11*, 119.
(36) Han, Y.; Oo, M. K.; Zhu, Y.; Sukhishvili, S.; Xiao, L.; Demohan, M. S.; Jinc, W.; Du, H. *Proc. SPIE* **2007**, *6767*, 67670G.
(37) Williamson, T. L.; Guo, X.; Zukoski, A.; Sood, A.; Diaz, D. J.; Bohn, P. W. *J. Phys. Chem. B* **2005**, *109*, 20186.
(38) Brolo, A. G.; Arctander, E.; Gordon, R.; Leathem, B.; Kavanagh, K. L. *Nano Lett.* **2004**, *4*, 2015.
(39) Yu, J.; Bai, X.; Suh, J.; Lee, S. B.; Son, S. J. *J. Am. Chem. Soc.* **2009**, *131*, 15574.
(40) Li, A. P.; Muller, F.; Birner, A.; Nielsch, A.; Gosele, U. *J. Appl. Phys.* **1998**, *84*, 6023.
(41) Foss, C. A., Jr; Hornyak, G. L.; Stockert, J. A.; Martin, C. R. *J. Phys. Chem.* **1994**, *98*, 2963.
(42) Saito, M.; Shibasaki, M.; Nakamura, S.; Miyagi, M. *Opt. Lett.* **1994**, *19*, 710.
(43) Lau, K. H. A.; Tan, S.; Tamada, K.; Sander, M. S.; Knoll, W. *J. Phys. Chem. B* **2004**, *108*, 10812.
(44) Kodiyath, R.; Wang, J.; Combs, Z. A.; Chang, S.; Gupta, M. K.; Anderson, K. D.; Brown, R. J. C.; Tsukruk, V. V. *Small* **2011**, *7*, 3452.
(45) Aggarwal, R. L.; Farrar, L. W.; Diebold, E. D.; Polla, L. *J. Raman Spectrosc.* **2009**, *40*, 1331.
(46) Zamuner, B. M.; Talaga, D.; Deiss, F.; Guieu, V.; Kuhn., A.; Ugo, P.; Sojic, N. *Adv. Funct. Mater.* **2009**, *19*, 3129.
(47) Sun, C. H.; Linn, N. C.; Jiang, P. *Chem. Mater.* **2007**, *19*, 4551.
(48) Masuda, H.; Fukuda, K. *Science* **1995**, *268*, 1466.
(49) Li, A. P.; Müller, F.; Birner, A.; Nielsch, K.; Gösele, U. *Adv. Mater.* **1999**, *11*, 483.
(50) See the Supporting Information for more detail
(51) Chang, S.; Combs, Z. A.; Gupta, M. K.; Davis, R.; Tsukruk, V. V. *ACS Appl. Mater. Interfaces* **2010**, *2*, 3339.
(52) Lee, W.; Scholz, R.; Nielsch, K.; Gosele, U. *Angew. Chem., Int. Ed.* **2005**, *44*, 6050.
(53) Tsukruk, V. V. *Rubber Chem. Technol.* **1997**, *70*, 430.
(54) McConney, M. E.; Singamaneni, S.; Tsukruk, V. V. *Polym. Rev.* **2010**, *50*, 235.
(55) Tsukruk, V. V.; Singamaneni, S. *Scanning Probe Microscopy of Soft Matter: Fundamentals and Practices*; Wiley-VCH, Weinheim, Germany, 2012.
(56) Singamaneni, S.; Gupta, M.; Yang, R.; Tomczak, M. M.; Naik, R. R.; Wang, Z. L.; Tsukruk, V. V. *ACS Nano* **2009**, *3*, 2593.
(57) Wales, D. J.; Doye, J. P. K.; Dullweber, A.; Hodges, M. P.; Naumkin F. Y.; Calvo, F.; Hernández-Rojas J.; Middleton, T. F. The

Cambridge Cluster Database. http://www-wales.ch.cam.ac.uk/CCD.html.

(58) Frisch, M. J.; Trucks, G. W.; Schlegel, H. B.; et al. *Gaussian 09*; Gaussian, Inc.: Wallingford, CT, 2009.

(59) Williams, S. D.; Johnson, T. J.; Gibbons, T. P.; Kitchens, C. L. *Theor. Chem. Acc.* **2007**, *117*, 283.

(60) Luo, L. B.; Chen, Li. M.; Zhang, M. L.; He, Z. B.; Zhang, W. F.; Yuan, G. D.; Zhang, W. J.; Lee, S. T. *J. Phys. Chem. C* **2009**, *113*, 9191.

(61) Kahl, M.; Voges, E.; Kostrewa, S.; Viets, C.; Hill, W. *Senss Actuators, A* **1998**, *51*, 285.

(62) Tessier, P. M.; Velev, O. D.; Kalambur, A. T.; Rabolt, J. F.; Lenhoff, A. M.; Kaler, E. W. *J. Am. Chem. Soc.* **2000**, *122*, 9554.

(63) Zhang, J.; Li, X.; Sun, X.; Li, Y. *J. Phys. Chem. B* **2005**, *109*, 12544.

(64) Jain, P. K.; Huang, W.; El-Sayed, M. A. *Nano Lett.* **2007**, *7*, 2080.

(65) Hohlbein, J.; Rehn, U.; Wehrspohn, R. B. *Phys. Status Solidi A* **2004**, *201*, 806.

(66) Mock, J. J.; Smith, D. R.; Schultz, S. *Nano Lett.* **2003**, *3*, 485.

(67) Evanoff, D. D., Jr.; Chumanov, G. *ChemPhysChem* **2005**, *6*, 1221.

(68) Michaels, A. M.; Nirmal, M.; Brus, L. E. *J. Am. Chem. Soc.* **1999**, *121*, 9932.

(69) Wang, W.; Gu, B. *Appl. Spectrosc.* **2005**, *12*, 1509.

(70) McFarland, A. D.; Young, M. A.; Dieringer, J. A.; Van Duyne, R. P. *J. Phys. Chem. B* **2005**, *109*, 11279.

(71) Jackson, j. B.; Halas, N. J. *Proc. Natl. Acad. Sci. U.S.A.* **2004**, *101*, 17930.

(72) Im, H.; Bantz, K. C.; Lindquist, N. C.; Hynes, C. L.; Oh, S. H. *Nano Lett.* **2010**, *10*, 2231.

(73) Wells, S. M.; Retterer, S. D.; Oran, J. M.; Sepaniak, M. J. *ACS Nano* **2009**, *3*, 3845.

(74) Gopinath, A.; Boriskina, S. V.; Premasiri, W. R.; Ziegler, L.; Reinhard, B. M.; Negro, L. D. *Nano Lett.* **2009**, *9*, 3922.

(75) Wang, W.; Raun, C.; Gu, B. *Anal. Chim. Acta* **2006**, *567*, 121.

(76) Futumata, M.; Maruyama, Y.; Ishikawa, M. *Vib. Spectrosc.* **2004**, *35*, 121.

(77) Yang, Xu.; Wheeler, D.; Newhouse, R.; Chen, B.; Zhang, J. Z.; Gu, C. *J. Opt. Soc. Am. A* **2010**, *27*, 977.

(78) Brown, R. J. C.; Milton, M. J. T. *J. Raman Spectrosc.* **2008**, *39*, 1313.

(79) Brown, R. J. C.; Wang, J.; Milton, M. J. T. *J. Nanomater.* **2007**, *2007*, 12086.

(80) Brown, R. J. C.; Wang, J.; Tantra, R.; Yardley, R. E.; Milton, M. J. T. *Faraday Discuss.* **2006**, *132*, 201.

(81) Tian, Z.-Q.; Ren, B. *J. Phys. Chem. B* **2002**, *106*, 9463.

(82) Saikin, S. K.; Amaya, R. O.; Rappoport, D.; Stopa, M.; Guzik, A. A. *Phys. Chem. Chem. Phys.* **2009**, *11*, 9401.

(83) Sato-Berru, R.; Redon, R.; Vazquez-Olmos, A.; Saniger, J. M. *J. Raman Spectrosc.* **2009**, *40*, 376.

(84) Otto, A.; Futamata, M. In *Electronic Mechanisms of SERS*; Kneipp, K., Moskovits, M., Kneipp, H., Eds.; Springer-Verlag: Berlin, Germany, 2006; Vol. *103*, Chapter 8, pp 147− 184.

(85) Morton, S. M.; Silverstein, D. W.; Jensen, L. *Chem. Rev.* **2011**, *111*, 3962.

(86) Jensen, L.; Aikens, C. M.; Schatz, G. C. *Chem. Soc. Rev.* **2008**, *37*, 1061.

(87) Lombardi, J. R.; Birke, R. L. *Acc. Chem. Res.* **2009**, *6*, 734.

(88) Jensen, L.; Zhao, L. L.; Schatz, G. C. *J. Phys. Chem. C* **2007**, *111*, 4756.

(89) Zhao, L. L.; Jensen, L.; Schatz, G. C. *Nano Lett.* **2006**, *6*, 1229.

(90) Zhao, L.; Jensen, L.; Schatz, G. C. *J. Am. Chem. Soc.* **2006**, *128*, 2911.

(91) Sun, M.; Liu, S.; Chen, M.; Xu, H. *J. Raman Spectrosc.* **2009**, *40*, 137.

(92) Jensen, L.; Zhao, L. L.; Schatz, G. C. *J. Phys. Chem. C* **2007**, *111*, 4756.

(93) Saikin, S. K.; Chu, Y.; Rappoport, D.; Crozier, K. B.; Guzik, A. A. *J. Phys. Chem. Lett.* **2010**, *1*, 2740.

(94) Liu, S.; Wan, S.; Chen., M.; Sun, M. *J. Raman Spectrosc.* **2008**, *39*, 1170−1177.

(95) Morton, S. M.; Jensen, L. *J. Am. Chem. Soc.* **2009**, *131*, 4090.

(96) Billmann, J.; Kovacs, G.; Otto, A. *Surf. Sci.* **1980**, *92*, 153.

(97) Dick, L. A.; McFarland, A. D.; Haynes, C. L.; Van Duyne, R. P. *J. Phys. Chem. B* **2002**, *106*, 853−860.

(98) Vivoni, A.; Birke, R. L.; Foucault, R.; Lombardi, J. R. *J. Phys. Chem. B* **2003**, *107*, 5547−5557.

(99) Gilman, J. J. *The Art and Science of Growing Crystals*; Wiley: New York, 1963; p 270.

(100) Brice, J. C. *J. Cryst. Growth* **1970**, *6*, 205.